Y/Hf-doped Al0.7CoCrFeNi high-entropy alloy with ultra oxidation and spallation resistance at 1200 °C

DOI:
10.1016/j.corsci.2020.108803

Document Version
Accepted author manuscript

Y/Hf-doped $Al_{0.7}CoCrFeNi$ high-entropy alloy with ultra oxidation and spallation resistance at 1200 °C

Jie Lu [a], Ying Chen [b], Han Zhang [a], Limin He [c], Rende Mu [c], Zaoyu Shen [c],

Xiaofeng Zhao [a,], Fangwei Guo [a]*

[a] *Shanghai Key Laboratory of Advanced High-Temperature Materials and Precision Forming, School of Materials Science and Engineering, Shanghai Jiao Tong University, Shanghai, 200240, China*

[b] *School of Materials, The University of Manchester, Manchester M13 9PL, United Kingdom*

[c] *Beijing Institute of Aeronautical Materials, Beijing, 100095, China*

Abstract

In this study, a new type of Y/Hf-doped $Al_{0.7}CoCrFeNi$ high-entropy alloy was fabricated and reported. Its oxidation behavior was investigated at 1200 °C compared with the conventional NiCoCrAlYHf alloy. The superior oxidation performance of the Y/Hf-doped $Al_{0.7}CoCrFeNi$ at 1200 °C is attributed to the dramatically enhancing homogeneity of Y/Hf-rich precipitates distribution at phase boundaries resulting from the intrinsic nano-sized phases in the alloy. The improving homogeneity of Y/Hf distribution is beneficial to inhibit the formation of interfacial imperfections and the interfacial S segregation, thus contributing to an enhancing interfacial adhesion and a strong resistance to TGO spallation.

Keywords: High-entropy alloy; Oxidation; Phase boundary; Y/Hf distribution

* Corresponding author: Xiaofeng Zhao (xiaofengzhao@sjtu.edu.cn)

1. Introduction

MCrAlY (M=Ni, Co or both) alloys are extensively used as the bond coat materials for thermal barrier coatings (TBCs), or protective overlay coatings for gas-turbines and aerospace engines blades to provide oxidation protection at high temperatures [1-6]. The oxidation resistance of these coatings relies on the capabilities to form a slow growing, well adherent α-Al_2O_3-based thermally grown oxides (TGO) at the coating surface after high-temperature oxidation [3, 7]. According to previous literatures, the oxidation of MCrAlY alloys are commonly investigated at/below 1100 °C and meanwhile the oxidation performance can be optimized by regulating compositions and microstructure of alloys [8-15].

In the practical case of blades of gas turbines or aerospace engines, the gas temperatures are constantly increasing to attain the requirement for the higher engine efficiency, thus the bond coats in TBCs and overlay coatings on the superalloy will endure a higher service temperature in the future [16]. Therefore, the investigation on the oxidation behavior for MCrAlY alloys at a higher temperature (e.g. 1200 °C) is critical to guiding the design for the advanced oxidation-resistant coatings, but has received only limited attention in previous literatures. It has been demonstrated by Ansari et al. that a considerable ratio of spallation and fracture of TGO occurred after merely three to ten cycles (10 h/cycle) at 1200 °C for the fully dense and thick (~600 μm) NiCrAlY coating manufactured through a laser-aided process [17]. These results indicate that the oxidation and spallation resistance of NiCrAlY coating at 1200 °C could not perhaps meet the requirement of long-term service for gas-turbines or aerospace engines. Thus it is of urgent necessity to develop an oxidation and spallation resistant coating material at 1200 °C for the purpose of matching the increasing gas temperatures in the gas-turbines or aerospace engines.

High-entropy alloys (HEAs) [18], have attracted constantly increasing attention because of their unique microstructure and adjustable properties [19-23]. In the last 10 years, two types of HEAs including single-phase face-centered cubic (FCC) HEAs and body-centered-cubic (BCC) HEAs have been widely investigated. However,

single-phase FCC HEAs (e.g. typical CrMnFeCoNi alloys) exhibit high tensile ductility but low yield strength [24-26]. Meanwhile, single BCC HEAs (e.g. typical NbMoTaW alloys) have extremely high strength but very low plasticity [27]. Therefore, multi-phase HEA (e.g. typical $Al_{0.7}$CoCrFeNi alloy) with a mixed structure of FCC and BCC is developed to achieve a balance between strength and ductility [28-31]. The mechanical properties of $Al_{0.7}$CoCrFeNi HEA at room temperatures substantially meet the criterion of a new type of bond coat material [30, 31]. Lim et al. [32] investigated the mechanical properties of dual-phase AlCoCrFeNi HEA at high temperature and found a higher high-temperature yield strength than the conventional NiCoCrAlY alloy [33].

However, only a few works have reported the oxidation performance of $Al_{0.7}$CoCrFeNi HEA. The oxidation behavior of as-cast $Al_{0.7}$CoCrFeNi HEA at 1050 °C has been investigated by Butler et al. [34, 35]. However, a thick Cr_2O_3-based TGO layer rather than a protective Al_2O_3-based TGO layer developed on the HEA surface. In addition, a weak TGO/metal interface adhesion and severe spallation of TGO occurred after a short oxidation time (e.g. 100 h). Since the doping of reactive elements (REs) in this alloy is not considered to improve its oxidation performance in these studies, the $Al_{0.7}$CoCrFeNi HEA exhibits an unsatisfactory oxidation performance once it is expected to be as an Al_2O_3-forming alloy. For the REs-doped NiCoCrAlY(Hf) and NiAlHf, typical Al_2O_3-forming alloys, the oxidation performance of these alloys can be significantly improved by the minor doping of REs (e.g. Y and Hf) due to the beneficial REs effects [36-39].

The overarching objective of this work is to investigate the oxidation performance of Y/Hf-doped $Al_{0.7}$CoCrFeNi HEA at an extremely high temperature (1200 °C) compared with the typical oxidation resistant NiCoCrAlYHf alloy. The test temperature of 1200 °C is selected to further highlight the superior oxidation performance of this Y/Hf-doped HEA. Additionally, the oxidation behavior of original HEA without Y/Hf-doping is studied for understanding the REs effects, while the oxidation tests at 1050 °C are also conducted for clarifying the temperature effect.

2. Materials and method

2.1. Material and sample preparation

Y/Hf-doped $Al_{0.7}CoCrFeNi$ high-entropy alloy (HEA) was designed and meanwhile the conventional NiCoCrAlYHf alloy (CNA) with typical compositions (referring to Amdry 365-2, Sulzer Metco) was also fabricated for comparison [40]. The chemical compositions (at.%) of the two as-cast alloys are given in Table 1. The high purity (99.99 wt.%) Al, Co, Cr, Fe, Ni, Y and Hf metals were placed on a water-cooled Cu hearth and then melted using arc melting under a high-purity argon atmosphere. The alloys were re-melted five times to obtain microstructural and compositional homogeneity.

Table 1. Chemical compositions (at.%) of two as-cast alloys.

Materials	Element (at.%)						
	Al	Co	Cr	Fe	Ni	Y	Hf
HEA	14.78	21.28	21.28	21.28	21.28	0.05	0.05
CNA	22.37	19.71	16.51	/	41.31	0.05	0.05

2.2. Isothermal oxidation test

A precision cut-off machine (Accutom 5, Struers) equipped with a SiC abrasive cutting blade was utilized to process the samples into square plates with a size of $10 \times 10 \times 3$ mm^3. All the samples were ground to a 1500-grit SiC finish following standard metallographic approaches. These samples were washed to remove stains using acetone and deionized water before oxidation. The isothermal oxidation experiment was conducted at 1050 °C and 1200 °C in a chamber furnace in the laboratory air for a successive exposure time (1 h to 300 h). The oxidation tests were performed using separate samples for each exposure time. The samples were placed in the center of the chamber furnace next to the thermocouple. Then, the samples were taken out from the furnace at 1050 °C and 1200 °C after a specific oxidation time, and then air cooling to room temperature outside the furnace in 10 min with the fan-assisted cooling method.

2.3. Characterization

The phase compositions of the alloy and TGO were studied using X-ray diffraction (XRD, Ultimo IV, Riau, Japan) at 30 kV with Cu Kα radiation. The spectra were collected in a 2θ range of 20~100° with a step size of 0.02° and a scanning speed of 0.5°/min. The morphologies of these samples were examined using scanning electron microscopy (SEM， FEI Nova Nano 230, Netherlands) and the chemical compositions were identified using energy dispersive X-ray spectroscopy (EDS, Oxford Instruments). To accurately identify the elemental composition and structure of each phase in the as-cast Y/Hf-doped $Al_{0.7}$CoCrFeNi high-entropy alloy, a focused ion beam (FIB, GAIA3, Tescan, Czech Republic) was employed to fabricate a thin lamella of this alloy with a thickness of about 50 nm and was subsequently characterized in detail using a transmission electron microscope (TEM, TALOS F200X, FEI, USA) equipped with an EDS system (XIS Ultra DLD, Kratos, Japan). The evolution of elemental concentration including S along the depth direction of TGO were collected using radiofrequency glow discharge optical emission spectroscopy (GD-OES, GDA750HP, Germany). The commercially available standard samples of each element is as a reference to obtain the actual concentration of each element at depth direction. The measuring residual stress in TGO was conducted at room temperature using photoluminescence piezospectroscopy (PLPS) on a confocal Raman microprobe (LabRAM HR, Horiba Jobin Yvon, France) with a 532 nm Nd:YAG laser. To accurately confirm the peak positions in each spectrum, all spectra were converted into the Labspec software 6.0 with an automatic fitting function using the mixed Gaussian-Lorentzian function.

3. Results

3.1. Microstructures of as-cast alloys

Fig. 1 shows the surface morphology of two as-cast alloys. As presented in Fig. 1a and b, CNA is a typical two-phase structure, comprising face-centered cubic (FCC) γ phase (bright contrast) and ordered body-centered cubic β (B2) phase (dark contrast), which

agrees well with the XRD results in Fig. 2 [3, 7, 40]. The average phase sizes of γ and β phases are about 20 μm and 5μm, respectively, which are defined by phase width. It should be noted that Y/Hf precipitates segregate to γ/β phase boundary resulting from the extremely low solubility of Y and Hf in the Ni-base superalloys [13, 38, 41-43]. As shown in Fig. 1c and d, a triple-phase structure can be observed in the HEA, which is also consistent with the XRD results in Fig. 2. In the solidified alloy, the white side plate phase is γ phase with a width of about 1μm. Between the side plate phase, a periodic, nano-sized structure consisting of alternating and interconnected disordered body-centered cubic (A2) phase and β phase (darkest contrast) with a width ranging from 100 nm to 500 nm can be seen (Fig. 1d). This type of structure can be attributed to the spinodal decomposition mechanism during the solidification [28]. It should be specially mentioned that fine Y/Hf precipitates (＜100 nm) are uniformly distributed at β/A2 phase boundaries (Fig. 1d). Chemical compositions of the phases in the two as-cast alloys determined by SEM-EDS point analysis are presented in Table 2. According to the Table 2, the γ phase is enriched with Ni, Co and Cr and the β phase is enriched with Ni and Al for the CNA. However, for the HEA, the compositions in the γ phase region and mixed region of A2 and β phase are basically similar, except for slight difference in the concentrations of Co and Cr. In short, the elemental distribution of HEA is much more uniform than that of CNA in terms of the SEM resolution.

Table 2. Chemical compositions (at.%) of the phases in the two as-cast alloys determined by SEM-EDS point analysis.

As-cast alloys	Phases	Elements (at.%)				
		Al	Co	Cr	Fe	Ni
CNA	γ	17.3	23.6	23.9	/	35.2
	β	38.4	14.1	8.9	/	38.6
HEA	γ	19.1	20.1	20.8	20.6	19.4
	A2+β	20.9	18.1	21.8	19.9	19.3

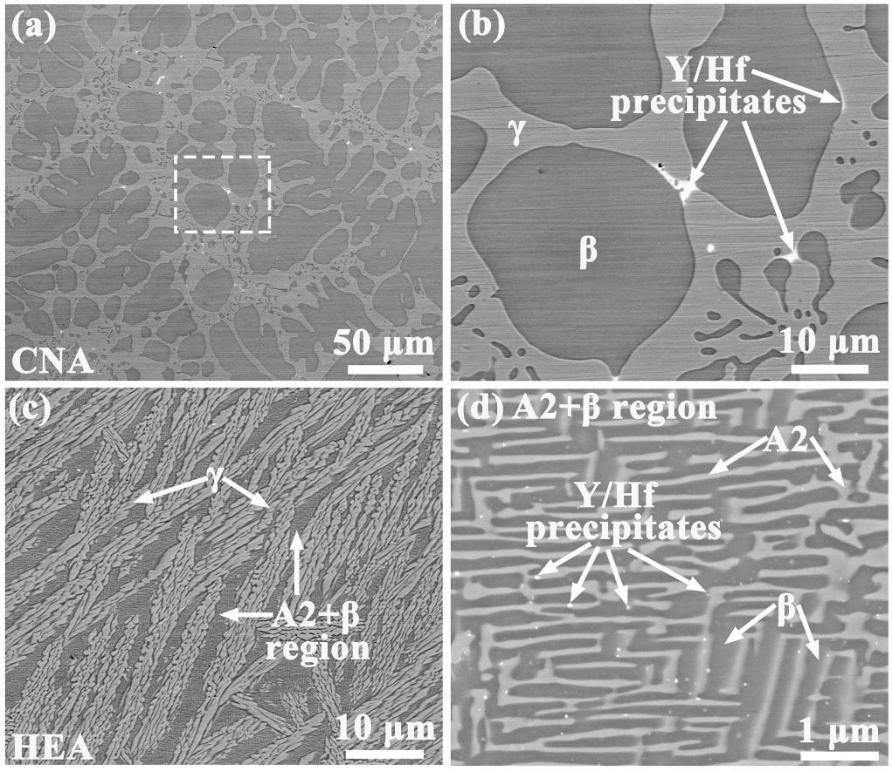

Fig. 1 Surface morphology of two as-cast alloys: (a) low magnification backscattered SEM (BSE) images, giving an overview of CNA; (b) high magnification BSE images over the area within the white rectangle in (a), showing the detail microstructure of CNA; (c) low magnification BSE images, showing a triple-phase microstructure in the HEA; (d) an amplifying BSE image in the mixed region of A2 and β phases in (c), showing the distribution of Y/Hf precipitates.

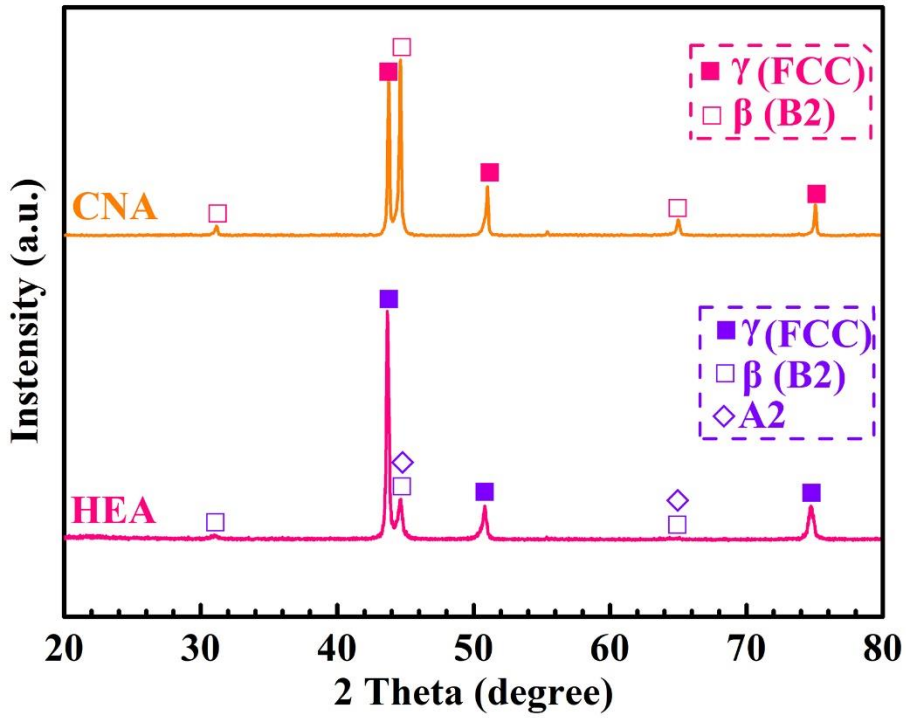

Fig. 2 XRD results of as-cast CNA and HEA

To reveal the composition and microstructure of HEA in greater detail, TEM analysis of HEA is presented in Fig. 3. It is clearly indicated through the HAADF-STEM image (Fig. 3a) combined with the SAED analysis (Fig. 3b and c) that the HEA comprises the γ phase with a FCC structure (brighest contrast), β phase with a B2 structure (darkest contrast) and A2 phase. The chemical compositions of three phases are recorded in Table 3 based on STEM-EDS point analysis. According to the Table 3, the distribution of Co is relatively uniform in the alloy. In addition, the γ phase is enriched with Fe,Cr and Ni, while β phase is NiAl-rich and the A2 phase is FeCr-rich. The Y/Hf precipitates are not seen in Fig. 3a, possibly due to the fairly small area of FIB-TEM sample or the loss of Y/Hf precipitates during ion milling.

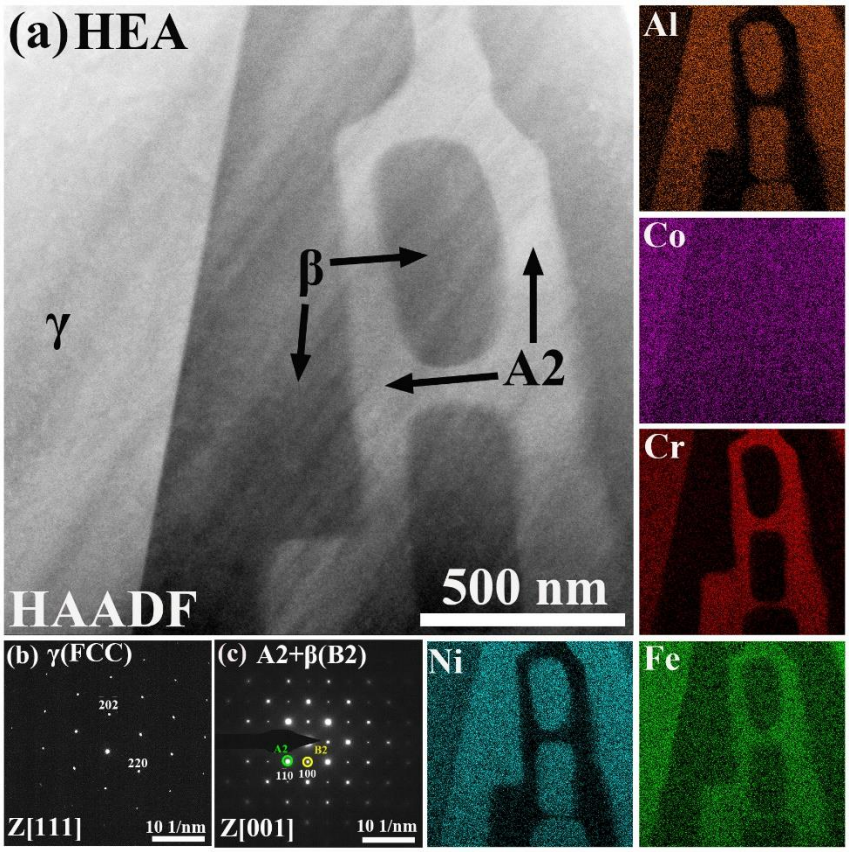

Fig. 3 TEM analysis of HEA: (a) high-angle annular dark-field (HAADF) STEM image with corresponding X-ray maps; (b) selected-area diffraction (SAED) patterns recorded from the γ phase region along the [111] zone axis, revealing a typical FCC structure; (c) selected-area diffraction (SAED) patterns recorded from the A2 + β (B2) phases region along the [001] zone axis, showing typical A2 and B2 structure.

Table 3. Chemical compositions (at.%) of γ, A2 and β phases in the HEA determined by quantitative STEM-EDS point analysis.

Phases	Element (at.%)				
	Al	Co	Cr	Fe	Ni
γ	5.1±0.8	23.4±2.7	25.2±2. 6	26.8±2.8	17.5±1.9
A2	3.9±0.5	20.6±2.9	40.3±4.5	28.1±3.7	7.1±1.4
β	30.5 ± 2.5	21.9±3.7	3.7±0.9	12.8±2.3	31.1±4.2

3.2. TGO spallation

The TGO spallation degree of two as-cast alloys with the increasing oxidation time is presented in Fig. 4. For the CNA, the exposed metal (bright region) reveals the locations of TGO spallation, which randomly distribute over the whole surface after 100 h and 300 h oxidation. The ratio of TGO spallation reaches 5% after 100 h oxidation and exceeds 15% after 300 h oxidation (Fig. 4a, b and e). Surprisingly, almost no TGO spallation can be found with the increasing oxidation time for the HEA and the intact TGO covers the overall surface after 300 h oxidation (Fig. 4c and d). In summary, the HEA exhibits significantly higher resistance to TGO spallation in comparison to the CNA at 1200 °C. To understand the difference in TGO spallation resistance between the two as-cast alloys, the TGO compositions, microstructures and interfacial morphology are systematically investigated as follows.

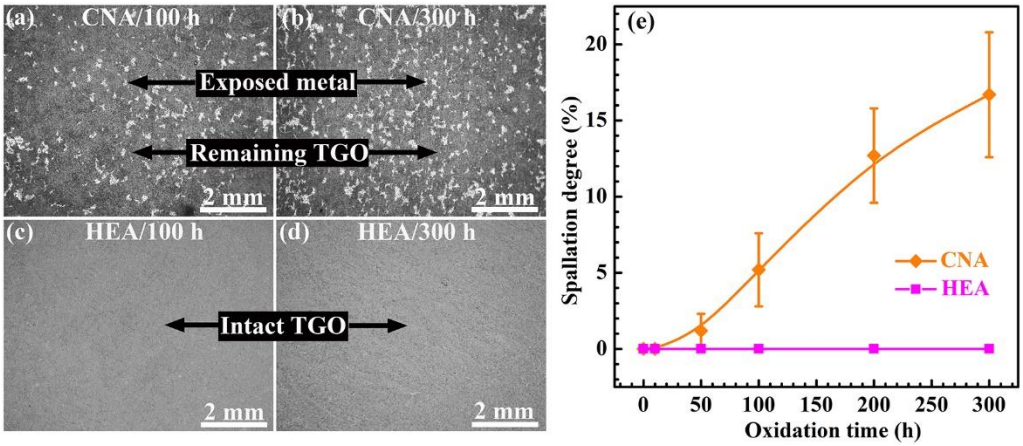

Fig. 4 (a, b) low magnification optical images, showing an overview of surface morphology of TGO formed on the CNA at 1200 °C after 100 h and 300 h, respectively; (c, d) low magnification optical images, showing an overview of surface morphology of TGO formed on the HEA at 1200 °C after 100 h and 300 h, respectively; (e) TGO spallation degree as a function of oxidation time at 1200 °C (The TGO spallation degree was defined by the ratio of the spalled area to the whole area of the TGO, which was measured using Image J software. Ten 500× magnification BSE micrographs were used to obtain the average spallation ratio of TGO and the error bar is the standard deviation[40].).

3.3. TGO compositions and microstructures

Fig. 5 shows the surface morphology of TGO formed on two as-cast alloys after 30 min oxidation at 1200 °C. As shown in Fig. 5a and b, the TGO morphology reveal two different regions, which inherit the original surface morphology of as-cast CNA (Fig. 1a and b). This result is possibly induced by compositional difference between γ phase and β phase, thereby leading to the difference in TGO morphology on the two phases after 30 min oxidation (Table 2). In addition, the Y/Hf-rich oxides are also observed at the boundary of two regions, due to the localized enrichment of Y/Hf precipitates from the γ/β phase boundaries (Fig. 1a and b). However, for the HEA (Fig. 5c and d), the TGO uniformly develops on the surface without the difference in morphology contrast as a result of the fine phase sizes (Fig. 5c and d) and uniform compositions (Table 2). Meanwhile, relatively fine Y/Hf-rich oxides randomly scatter on the TGO surface. The fast establishment of uniform scale in the early oxidation stage for the HEA is beneficial to mechanical integrity of TGO.

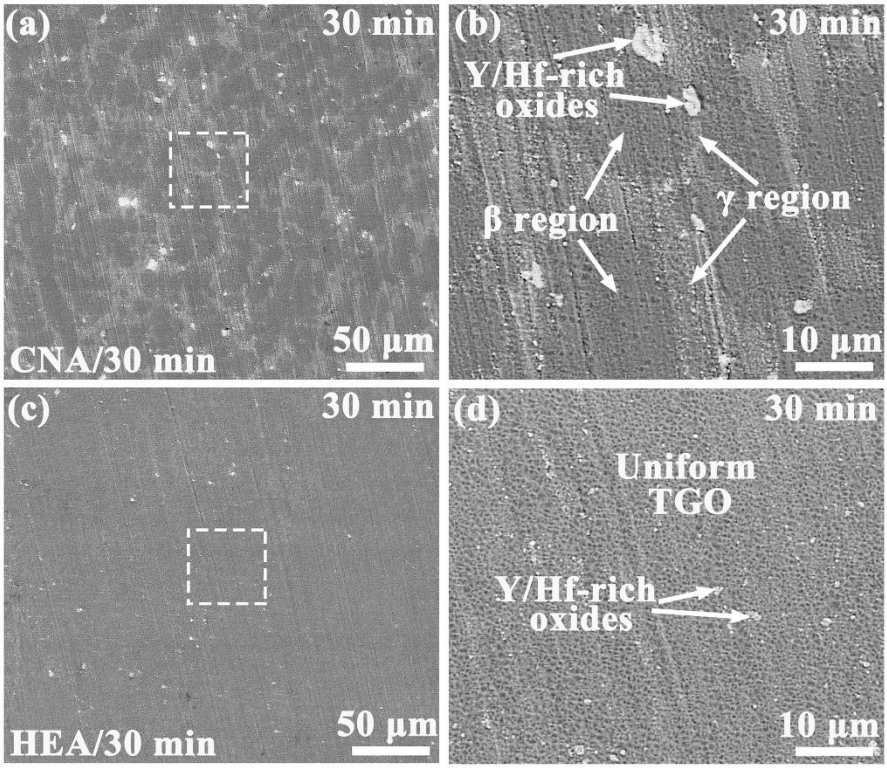

Fig. 5 Surface morphology of TGO formed on the two as-cast alloys after oxidation for 30 min at 1200 °C: (a, c) low magnification BSE images, giving an overview of TGO surface for the CNA and HEA, respectively; (b, d) high magnification BSE images over

the area within the white rectangle in (a, c), showing the detail microstructure of TGO for the CNA and HEA, respectively.

Fig. 6 shows the surface morphology of two as-cast alloys after 300 h oxidation at 1200 °C. For the CNA (Fig. 6a and b), the exposed metal surface and remaining oxide intrusions (also termed as thickness imperfections) embedded into metal substrate at the spalled region indicate that the TGO spallation predominantly occurs at TGO/metal interface and surrounding the Y/Hf-rich intrusion imperfections [13, 43-46]. Additionally, Y/Hf-rich oxides are detected at the Al_2O_3 grain boundaries from the TGO surface away from the spalled region (Fig. 6c). For the HEA (Fig. 6d and e), no TGO spallation can be found and meanwhile the TGO surface is uniform and smooth, which show a superior resistance to TGO spallation. It can be clearly seen that Y/Hf-rich oxides also segregate at the Al_2O_3 grain boundaries for the HEA (Fig. 6f). Nevertheless, the Y/Hf-rich oxides have finer size and more uniform distribution over the whole TGO surface in comparison to those of CNA, which can be associated with the uniform segregation of Y/Hf precipitates to phase boundaries in the HEA. As the XRD results presented in Fig. 7, the TGO primarily consists of α-Al_2O_3 accompanied by minor amount of Y/Hf-rich oxides, while the Y/Hf-rich oxides are identified to be $Y_3Al_5O_{12}$ and HfO_2. In addition, the high diffraction intensity of γ-peak from the HEA also indicates severe spallation of TGO and exposure of metal substrate occur after 300 h oxidation. These results are well in agreement with surface morphology shown in Fig. 6a.

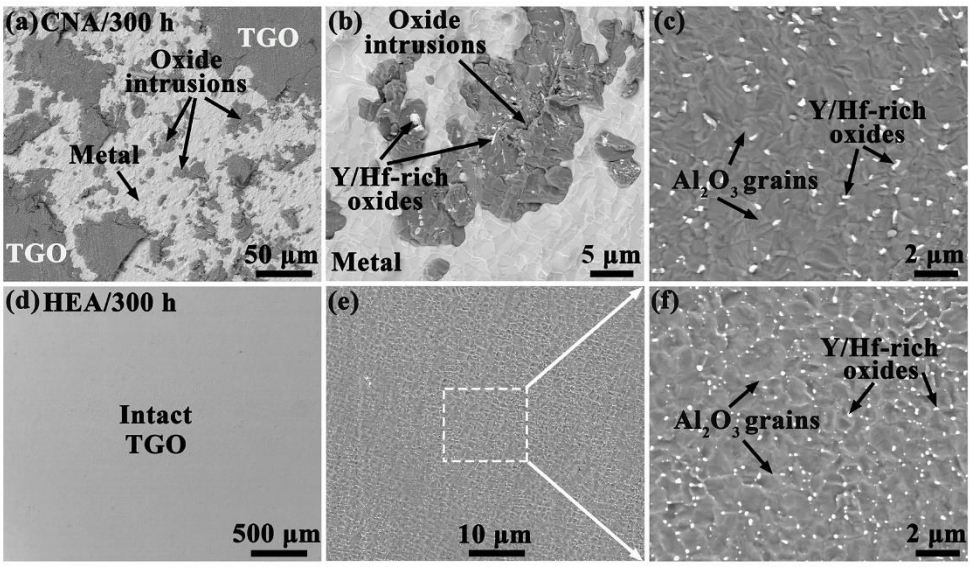

Fig. 6 Surface morphology of two as-cast alloys after oxidation for 300 h at 1200 °C: (a) an overview of the TGO surface for the CNA; (b) a typical oxide intrusions extended into the CNA substrate; (c) surface microstructure of TGO away from the spalled region for the CNA; (d) an overview of the TGO surface, showing the intact TGO for the HEA; (e, f) high magnification surface microstructure of TGO for the HEA.

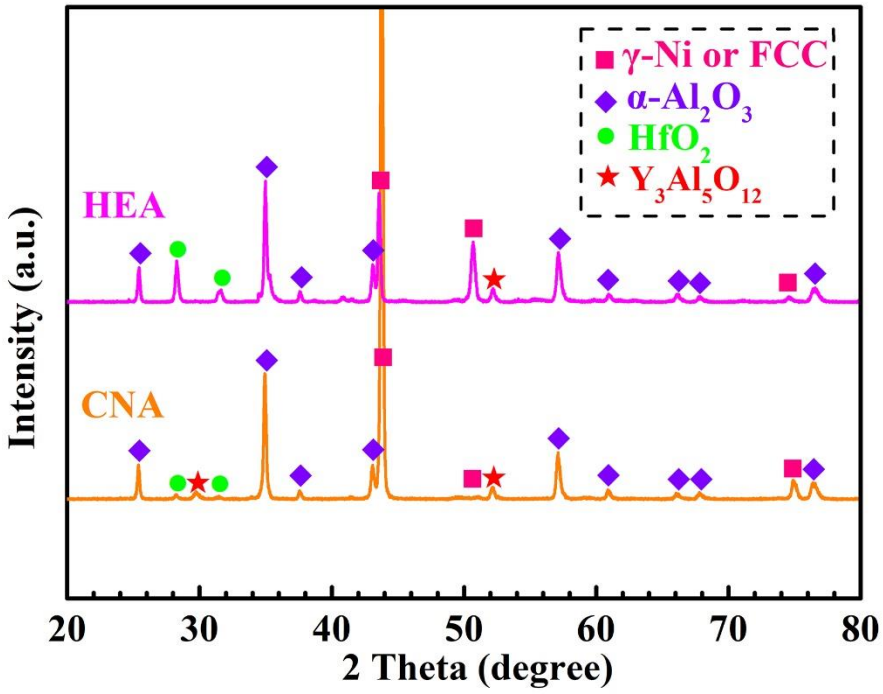

Fig. 7 XRD results of two as-cast alloys after oxidation for 300 h at 1200 °C.

Fig. 8 shows the cross-sectional microstructure of two as-cast alloys after oxidation for 300 h at 1200 °C. For the CNA, the interfacial detachment can be observed near the spalled region, while the detached interface also occurs primarily around the Y/Hf-rich

oxide intrusions away from the spalled region (Fig. 8a and b). In addition, interfacial pores are also seen in vicinity of oxide intrusions, which is probably induced by the volume shrinkage deriving from the transformation of α-Al_2O_3 to $Y_3Al_5O_{12}$ (Fig. 8b). These results suggest that TGO delamination is closely connected with the oxide intrusions and pores at interface for the CNA. While, for the HEA, the TGO is well adherent with the metal substrate and no interfacial detachment, cracks or pores can be detected, which reveal a strong interfacial bonding. Meanwhile, some fine Y/Hf-containing oxides (defined as pegs) form at interface, which is believed to be beneficial to mechanically anchoring the TGO layer, and thus increases the interfacial adhesion [47]. Although the transformation and coarsening of phases is inevitable after long-term oxidation for two alloys (Fig. 8a and c), the formation of oxide intrusions at TGO/metal interface relies on the early oxidation stage, which is predominantly affected by the original alloy microstructure [15, 48, 49]. It should be also mentioned that the oxidation kinetics after long-term oxidation are basically consistent for two as-cast alloys due to almost equal TGO thickness (about 6.2 μm after 300 h oxidation) (Fig. 8b and d).

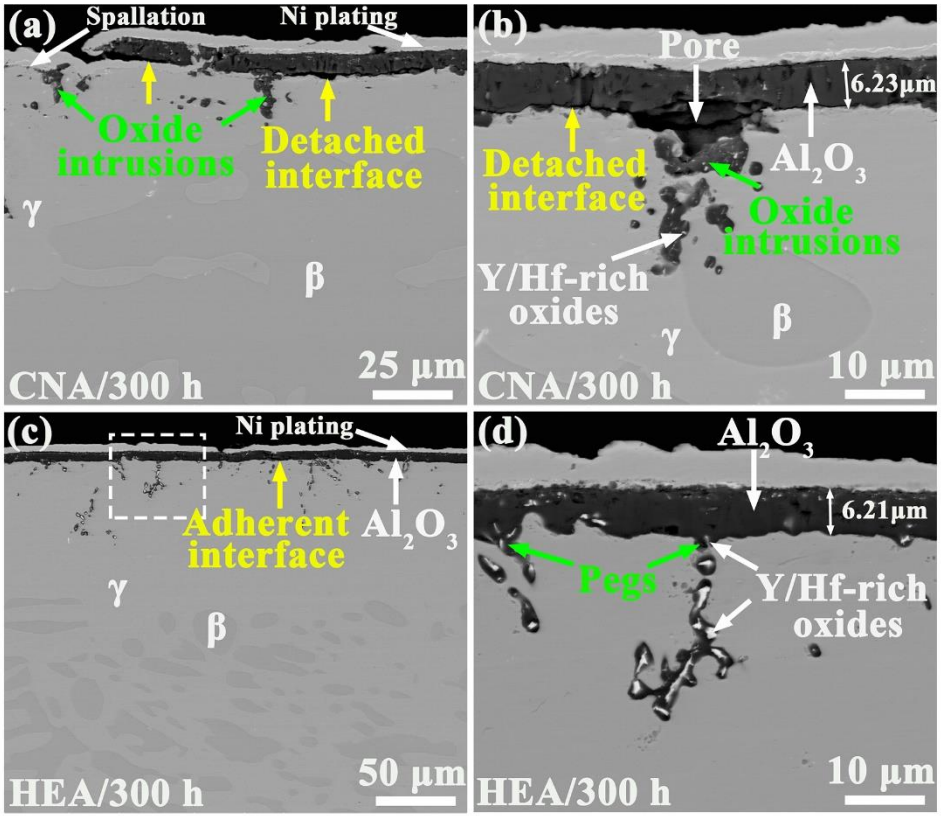

Fig. 8 Cross-sectional morphology of two as-cast alloys after oxidation for 300 h at

1200 °C: (a) cross-sectional morphology of TGO near the spalled region for the CNA; (b) cross-sectional TGO morphology away from the spalled region for the CNA; (c) low magnification cross-sectional TGO morphology and (d) high magnification cross-sectional TGO morphology over the area within the white rectangle in (c) for the HEA.

4. Discussion

4.1. Oxidation behavior at 1050 °C and 1200 °C

It is clearly presented in Fig. 5-7 that TGO formed on the HEA with Y/Hf doping predominantly consists of Al_2O_3 and is well adherent with the alloy substrate at 1200 °C. However, Butler and Weaver observed thick Cr_2O_3 scale formation and dispersive AlN formation near interface at 1050°C for the same Al-containing HEA without Y/Hf doping [34]. To clarify the effect of temperature on TGO growth for the HEA, the oxidation experiments of HEA without Y/Hf doping at 1050 °C were also conducted in this study. Fig. 9 shows surface and cross-sectional TGO morphology of HEA without Y/Hf doping after 100 h oxidation at 1050 °C. As show in Fig. 9a, a large amount of interfacial pores and severe TGO spallation can be observed after oxidation. The interfacial pores can weaken interface adhesion and thus induce the premature scale failure [38]. It should be noted that the TGO primarily comprises continuous Al_2O_3 scale and only minor and tiny spinel can be found on the TGO surface (Fig. 9b-d). In addition, the spinel contains all base elements in combination with the elemental maps and no Cr_2O_3 and AlN can be seen. Based on the results above, the HEA ($Al_{0.7}$CoCrFeNi) is an Al_2O_3-forming alloy, while the minor spinel perhaps derives from the local inhomogeneity of composition during arc melting. But the weak interfacial adhesion due to the absence of Y/Hf causes extremely inferior resistance to TGO spallation (Fig. 9a).

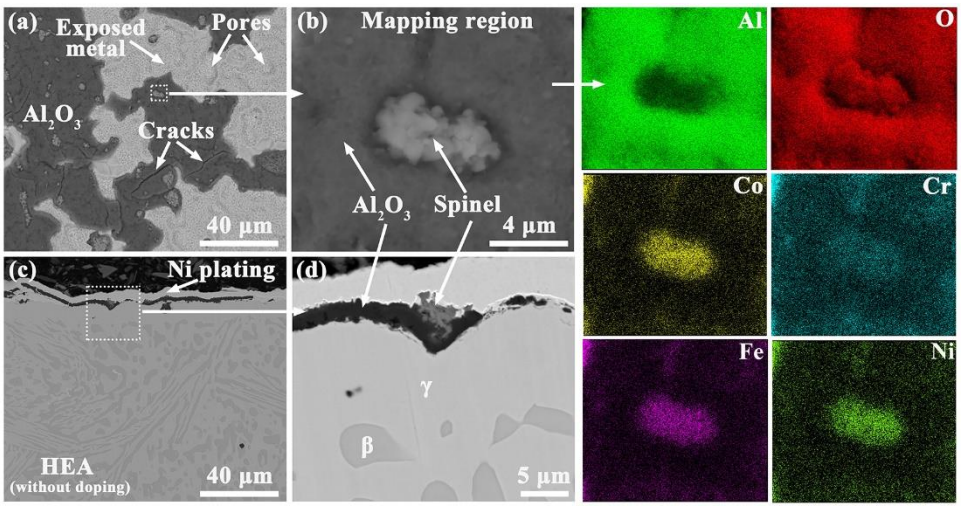

Fig. 9 Surface and cross-sectional morphology of HEA without Y/Hf doping after oxidation for 100h at 1050 °C: (a) low magnification BSE image, giving an overview of TGO surface; (b) high magnification BSE images over the area within the white rectangle in (a) and corresponding elemental maps, showing the TGO composition; (c) low magnification BSE image and (d) amplifying area within the white rectangle in (c), showing the cross section of TGO.

In addition to the oxidation of HEA without Y/Hf doping at 1050 °C, the oxidation behavior of HEA with Y/Hf doping at 1050 °C is also investigated to highlight the necessity of RE doping for designing oxidation and spallation resistant alloy. Fig. 10 shows surface and cross-sectional TGO morphology of HEA with Y/Hf doping after 100 h oxidation at 1050 °C. It can be clearly seen that the TGO is uniform and continuous Al_2O_3 scale accompanied with the uniform distribution of Y/Hf-rich oxides at scale grain boundary. More importantly, the TGO exhibits a strong interfacial adhesion and no TGO spallation can be observed after 100 h oxidation at 1050 °C. Moreover, fine oxide pegs form at interface due to Y/Hf doping, which are effective to resist the separation of the interface, thereby strengthening the interfacial bonding [50]. Based on the results above, it can be concluded that RE (Y/Hf) addition is indispensable for developing an oxidation and spallation resistant HEA, while the TGO formed on the Y/Hf-doped HEA is preferential Al_2O_3 formation in spite of either temperature (1050 °C or 1200 °C). The overarching objective of this study is to develop a high-performance Al_2O_3-forming alloy at 1200 °C, which is superior to the conventional

NiCoCrAlYHf alloy. Therefore, the following section focuses on discussing the failure mechanism of TGO for the Y/Hf-doped HEA at 1200 °C compared with the NiCoCrAlYHf alloy.

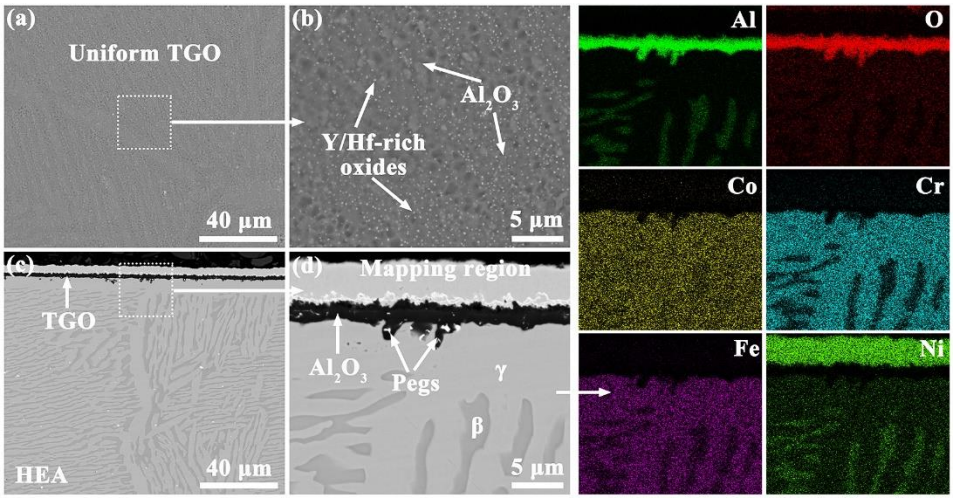

Fig. 10 Surface and cross-sectional morphology of HEA with Y/Hf doping after oxidation for 100h at 1050 °C: (a) low magnification BSE image, giving an overview of TGO surface; (b) high magnification BSE images over the area within the white rectangle in (a), showing the detailed grain structure; (c) low magnification BSE image, showing the continuous TGO growth; (d) amplifying area within the white rectangle in (c) and corresponding elemental maps, showing the TGO composition.

4.2. Spallation mechanism of TGO at 1200 °C

It is well documented that TGO delamination is predominantly driven by the elastic strain energy stored in TGO G, which constantly increases with the increasing TGO thickness h_{ox}. Once G surpasses the interfacial toughness G_c, the delamination of TGO from interface will occur, which can be represented by [51]:

$$G=\frac{1-\nu_{ox}^2}{2E_{ox}}\bar{\sigma}^2 h_{ox} \qquad (1)$$

where E_{ox} and ν_{ox} are Young' modulus and Poisson' ratio of TGO, respectively. The TGO residual stress $\bar{\sigma}$ can be measured at room temperature, using PLPS technique, by [47, 52]

$$\Delta\upsilon=5.07\overline{\sigma} \qquad (2)$$

where $\Delta\upsilon$ is the peak shift from alumina R2 line, using a stress-free sapphire as a stress reference . The residual stress predominantly comes from the thermal expansion mismatch stress between the TGO and metal substrate and growth stress accompanied by stress relaxation [44].

Fig. 11 shows the TGO residual stress collected from the intact TGO region with the increasing oxidation time for the two as-cast alloys. In the initial oxidation stage (＜25 h), the initially slight increases in the residual stress for the two-cast alloys are likely to derive from the homogenization process of TGO growth [53]. For the subsequent oxidation time until 300 h, the TGO residual stress keeps highly stable (6.6±0.4 GPa) for the two-cast alloys. In short, the two alloys show negligible difference in the TGO residual stress in spite of the cumulative oxidation time. Consequently, the driving force for TGO delamination determining by TGO residual stress (Fig. 11) and TGO thickness (Fig. 8b and d) for the two as-cast alloys is substantially equal according to the Equation (1). It is extensively accepted that the constantly increasing elastic strain energy actuates TGO delamination, and in turn the interfacial toughness suppresses this detrimental process [51]. Therefore, the tremendous difference in the resistance to TGO spallation for two-cast alloys is mainly controlled by interfacial toughness on the account of the negligible difference in the driving force of delamination.

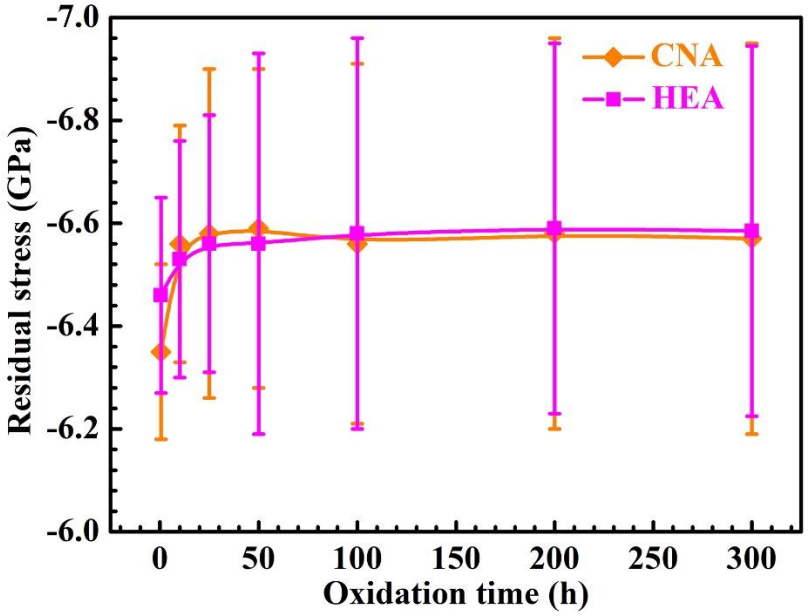

Fig. 11 Difference of residual stress in TGO with the cumulative oxidation time at 1200 °C for the two as-cast alloys. Each solid symbol in this figure represents the average value of 500 measurements, which is measured using separate samples. The error bar represents the standard deviation of 500 measurements.

In general, the interfacial toughness is predominantly affected by both the intrinsic impurity segregation to TGO/metal interface (e.g. S segregation) and interfacial imperfections (e.g. oxide intrusions and interfacial pores) [41, 44, 45, 54-57]. It has been well demonstrated in previous works that REs can tie up S and suppress the interfacial segregation, thereby improving the interfacial toughness [38, 44, 58]. To examine the interfacial segregation of S, the distribution of S and other corresponding elements across TGO surface to the as-cast alloy substrate are collected using GD-OES, which is a powerful technique to quantitatively analyze elemental distribution along depth direction for multilayer materials [38, 59]. Fig. 12 shows the evolution of elemental concentration along the depth direction of TGO for the two as-cast alloys after 300 h oxidation at 1200 °C. For the CNA (Fig. 12a), the S concentration increases quickly from the TGO surface to TGO interior, attaining a maximal amount at the TGO/CNA metal interface, and subsequently declines to zero when the sputtering depth exceeds interface. For the HEA (Fig. 12b), the S is only detected inside TGO with a depth of about 1μm from the TGO surface to TGO interior and meanwhile no S can be found at the TGO/HEA substrate interface. Similar segregation of S in the TGO interior rather than the interfacial segregation of S is also observed in the Hf-doped NiAl alloy, which exhibits a strong TGO/metal interface bonding after oxidation at 1150 °C [38]. In short, the interfacial segregation of S is well inhibited after oxidation for the HEA. These results completely differ from the primary interface segregation of S for the CNA. Since the doped concentration of REs in the two as-cast alloys is same, the stronger inhibiting effect of interfacial S segregation for the HEA could result from the enhancing homogeneity of REs distribution in comparison to that for the CNA (Fig. 1 and 6). It was also mentioned by Nijdam et al. that the improving homogeneity of Y distribution in the NiCoCrAlY alloy can further inhibit the segregation of S to interface [48]. It is also demonstrated in our previous work that uniform distribution of Y in the

NiCoCrAlY alloy fabricated using the milling powder can effectively suppress the interfacial S segregation during high-temperature oxidation [52]. In theory, the S is quickly saturated at the attached TGO/metal interface at high temperature and thus will transfer into TGO [55, 60]. Actually, the S is also easily enriched on the surface of interface pores [38]. For the CNA, a peak value of S concentration occurs at the TGO/metal interface, probably deriving from both the saturated S at the attached interface and the enriched S on the surface of interface pores (Fig. 8b and 10a). For the HEA, the uniform distribution of REs inhibits the interfacial S segregation and thereby increases the interfacial toughness.

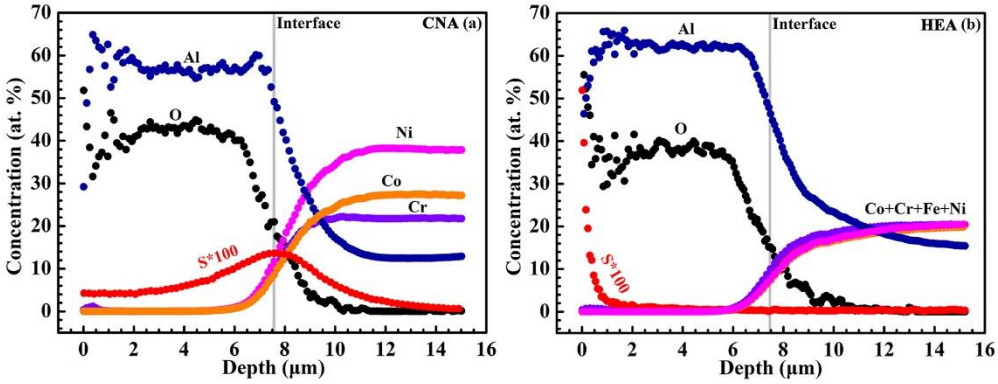

Fig. 12. Evolution of elemental concentration across the TGO surface to the metal substrate collected using GD-OES technique for two as-cast alloys after oxidation at 1200 °C for 300 h: (a) CNA; (b) HEA. (The depth profiles of Y and Hf are not recorded in this figure, due to the absence of the standard sample. S*100 represents that the value presented in this figure is 100-time higher than that of actual S concentration. Values of other corresponding elements represent the actual concentration.)

Apart from the interfacial S segregation, the interfacial imperfections including oxide intrusions and interfacial pores are also of importance to degrading the interfacial toughness [44, 51]. For the CNA, the localized enrichment of Y/Hf-precipitates at γ/β phase boundaries due to its relatively large phase sizes causes the extension of Y/Hf-rich oxide intrusions into metal substrate (Fig. 6a and b). Furthermore, the Y/Hf-rich oxide intrusions will develop and enlarge quickly with the increasing oxidation time due to the faster O transport rate in the Y/Hf-rich oxides than that in the Al_2O_3 [44, 45, 49]. The only imperfections of possibly inducing interfacial detachments at the exposed

metal surface are the intrusion imperfections, which are believed to be the original nucleation sites of interfacial detachments or cracks. The intrusion imperfections lead to stress concentration due to the local volume expansion at interface, thereby easily nucleating cracks in the vicinity of imperfections (Fig. 8a and b) [44, 45, 51]. Moreover, interfacial pores are also observed in the vicinity of the oxide intrusions, which will reduce the contact area of interface and thus lower the interfacial toughness.

With the cumulative oxidation time at a high temperature, the high concentration of interfacial S segregation will degrade the interfacial toughness quickly. In this case, the persistently coarsening intrusion imperfections at interface and interfacial pores can cause easily interfacial detachments or cracks as a consequence of the rapid weakening of interfacial adherence.

For the HEA, the Y/Hf-precipitates are uniformly distributed at phase boundaries owing to the fine or nano-sized phase constitutions (Fig. 1c and d). Consequently, no large Y/Hf-rich oxide intrusions form at TGO/metal interface to induce the nucleation of interfacial imperfections, thereby effectively maintaining the interfacial toughness (Fig. 8c and d). Meanwhile, some fine oxide pegs occurring at interface can enhance the interfacial adhesion (Fig. 8c and d). In conclusion, the absence of interfacial imperfections, the presence of fine oxide pegs at interface and strong inhibition of interfacial S segregation guarantee a strong interfacial adhesion for the HEA, thus contributing to an ultra resistance to TGO spallation compared with that of CNA at 1200 °C.

5. Outlook

REs (e.g. Y or Hf) are commonly doped into the CNA to improve its oxidation performance due to the beneficial REs-effects. First, REs actively react with and tie up with S or C, and thus prevent their segregation to interface and maintains the interfacial adhesion [61, 62]. Second, the segregation of REs ions to TGO grain boundaries can inhibit the outward Al diffusion from the underlying alloy, thereby slowing down the TGO growth rate [63]. However, two detrimental effects have been always mentioned

with the increasing REs content in the previous literatures, which are summarized as follows: (1) the incorporation of a large amount of REs oxides inevitably increases the oxidation rate because of the much faster O diffusivity in REs oxides than that in Al_2O_3 [13, 43, 46, 64]; (2) large-sized REs-rich oxide intrusions form at interface due to the localized enrichment of REs precipitates in the alloy, which can easily lead to the nucleation of interfacial cracks, and thus degrade the interfacial adhesion [44, 51]. Therefore, how to maximize the beneficial REs-effects should be an important issue for improving the oxidation performance of Al_2O_3-forming alloy.

The $Al_{0.7}$CoCrFeNi HEA used in this study could provide a solution, which is the homogenization of REs in the alloy. The nano-sized phases in the HEA can contribute to a large number of sites for the segregation of REs due to the high density of phase boundaries, thereby homogenizing the REs distribution. Once REs are uniformly distributed in the alloy, the detrimental effects could be eliminated. Therefore, the beneficial REs-effects will be expected to maximize through a combination of the increase of REs content and the high density of phase boundaries in the alloy. In other words, the HEA presented in this study exhibits a huge potential in maximizing the beneficial REs-effects, and thereby significantly increases its possibility to be used at an extremely high temperature (e.g. 1200 °C). Additionally, the phase constitutions, distribution, size and shape will be changed by altering the Al content in the Al_xCoCrFeNi high-entropy alloy [28]. Therefore, the distribution of REs in the alloy will be also affected due to a different Al content, which will be reported in our later works.

6. Conclusions

In the present study, an ultra oxidation and spallation reisitant Y/Hf-doped $Al_{0.7}$CoCrFeNi high-entropy alloy (HEA) was reported and meanwhile its oxidation behavior was systematically inveastigated at 1200 °C compared with that of conventional NiCoCrAlYHf alloy (CNA).

(1) The HEA without Y/Hf doping is an Al_2O_3-forming alloy, but this alloy exhibits

extremely inferior TGO spallation resistance due to the lack of Y/Hf doping. More importantly, the TGO spallation resistance of this HEA can be significantly improved through the addition of Y/Hf. Thus RE (Y/Hf) addition is indispensable for ensuring the superior oxidation and spallation resistance of this HEA.

(2) For the CNA, localized enrichment of Y/Hf precipitates at phase boundaries due to relatively large phase sizes leads to the formation of large-sized Y/Hf-rich oxide intrusions at TGO/metal interface. For the HEA, Y/Hf precipitates are uniformly distributed at phase boundaries owing to the nano-sized phase constitutions, which inhibits the occurrence of interfacial imperfections at TGO/metal interface.

(3) For the CNA, the predominant S impurity to TGO/metal interface is observed, probably resulting from the the saturated S at the attached interface and the enriched S on the surface of interface pores. For the HEA, the interfacial S segregation is thoroughly suppressed and the S is only detected in the TGO interior, which are attributed to the uniform distribution of reactive elements (e.g. Y and Hf) in the alloy.

(4) Y/Hf-rich oxide intrusions are proposed to be initial sites of interfacial detachments or pores for the CNA, which lead to the rapid degradation of interfacial adhesion. For the HEA, no interfacial imperfections form at TGO/metal interface, and in turn some fine oxide pegs at interface can enhance the interfacial adhesion.

(5) The superior resistance to TGO spallation for the HEA is eventually attributed to the strong interfacial adhesion, which is induced by the absence of interfacial imperfections, the presence of fine oxide pegs at interface and strong inhibition of interfacial S segregation.

In summary, the HEA exhibits tremendous potential in applications for the oxidation resistant protective overlay coating or bond coat material in TBCs with the increasing gas temperature, in terms of the ultra oxidation and spallation resistance at 1200 °C. Further works are in progress to optimize the oxidation performance through modifying the compositions (e.g. species and content of reactive elements or Al content).

Acknowledgements

This work was financially supported by National Natural Science Foundation of China (51971139).

References

[1] N.P. Padture, M. Gell, E.H. Jordan, Thermal barrier coatings for gas-turbine engine applications, Science, 296 (2002) 280-284.

[2] A.G. Evans, M.Y. He, J.W. Hutchinson, Mechanics-based scaling laws for the durability of thermal barrier coatings, Prog. Mater. Sci. 46 (2001) 249-271.

[3] M.J. Pomeroy, Coatings for gas turbine materials and long term stability issues, Mater. Des. 26 (2005) 223-231.

[4] Q. Shen, L. Yang, Y.C. Zhou, Y.G. Wei, N.G. Wang, Models for predicting TGO growth to rough interface in TBCs, Surf. Coat. Technol. 325 (2017) 219-228.

[5] Q. Shen, S.Z. Li, L. Yang, Y.C. Zhou, Y.G. Wei, T. Yuan, Coupled mechanical-oxidation modeling during oxidation of thermal barrier coatings, Comput. Mater. Sci.154 (2018) 538-546.

[6] Q. Shen, L. Yang, Y.C. Zhou, Y.G. Wei, W. Zhu, Effects of growth stress in finite-deformation thermally grown oxide on failure mechanism of thermal barrier coatings, Mech. Mater. 114 (2017) 228-242.

[7] Y. Chen, X. Zhao, P. Xiao, Effect of microstructure on early oxidation of MCrAlY coatings, Acta Mater. 159 (2018) 150-162.

[8] A. Gil, V. Shemet, R. Vassen, M. Subanovic, J. Toscano, D. Naumenko, L. Singheiser, W.J. Quadakkers, Effect of surface condition on the oxidation behaviour of MCrAlY coatings, Surf. Coat. Technol. 201 (2006) 3824-3828.

[9] E. Hejrani, D. Sebold, W.J. Nowak, G. Mauer, D. Naumenko, R. Vaßen, W.J. Quadakkers, Isothermal and cyclic oxidation behavior of free standing MCrAlY coatings manufactured by high-velocity atmospheric plasma spraying, Surf. Coat. Technol. 313 (2017) 191-201.

[10] J. Toscano, A. Gil, T. Hüttel, E. Wessel, D. Naumenko, L. Singheiser, W.J. Quadakkers, Temperature dependence of phase relationships in different types of MCrAlY-coatings, Surf. Coat. Technol. 202 (2007) 603-607.

[11] K.A. Unocic, B.A. Pint, Characterization of the alumina scale formed on a commercial MCrAlYHfSi coating, Surf. Coat. Technol. 205 (2010) 1178-1182.

[12] H. Peng, H. Guo, J. He, S. Gong, Microscale lamellar NiCoCrAlY coating with improved oxidation resistance, Surf. Coat. Technol. 207 (2012) 110-116.

[13] T.J. Nijdam, W.G. Sloof, Effect of reactive element oxide inclusions on the growth kinetics of protective oxide scales, Acta Mater. 55 (2007) 5980-5987.

[14] R. Chen, X. Gong, Y. Wang, G. Qin, N. Zhang, Y. Su, H. Ding, J. Guo, H. Fu, Microstructure and oxidation behaviour of plasma-sprayed NiCoCrAlY coatings with and without Ta on Ti44Al6Nb1Cr alloys, Corros. Sci. 136 (2018) 244-254.

[15] T.J. Nijdam, L.P.H. Jeurgens, J.H. Chen, W.G. Sloof, On the Microstructure of the Initial Oxide Grown by Controlled Annealing and Oxidation on a NiCoCrAlY Bond Coating, Oxid. Met. 64 (2005) 355-377.

[16] D.R. Clarke, M. Oechsner, N.P. Padture, Thermal-barrier coatings for more efficient gas-turbine engines, MRS Bulletin, 37 (2012) 891-898.

[17] M. Ansari, R. Shoja-Razavi, M. Barekat, H.C. Man, High-temperature oxidation behavior of laser-aided additively manufactured NiCrAlY coating, Corros. Sci. 118 (2017) 168-177.

[18] J.W. Yeh, S.K. Chen, S.J. Lin, J.Y. Gan, T.S. Chin, T.T. Shun, C.H. Tsau, S.Y. Chang, Nanostructured High-Entropy Alloys with Multiple Principal Elements: Novel Alloy Design Concepts and Outcomes, Adv. Eng. Mater. 6 (2004) 299-303.

[19] D.B. Miracle, O.N. Senkov, A critical review of high entropy alloys and related concepts, Acta Mater. 122 (2017) 448-511.

[20] Y.F. Ye, Q. Wang, J. Lu, C.T. Liu, Y. Yang, High-entropy alloy: challenges and prospects, Materials Today, 19 (2016) 349-362.

[21] Y. Zhang, T.T. Zuo, Z. Tang, M.C. Gao, K.A. Dahmen, P.K. Liaw, Z.P. Lu, Microstructures and properties of high-entropy alloys, Prog. Mater. Sci. 61 (2014) 1-93.

[22] Z. Li, S. Zhao, R.O. Ritchie, M.A. Meyers, Mechanical properties of high-entropy alloys with emphasis on face-centered cubic alloys, Prog. Mater. Sci. 102 (2019) 296-345.

[23] Z. Li, Interstitial equiatomic CoCrFeMnNi high-entropy alloys: carbon content, microstructure, and compositional homogeneity effects on deformation behavior, Acta Mater. 164 (2019) 400-412.

[24] Y. Deng, C.C. Tasan, K.G. Pradeep, H. Springer, A. Kostka, D. Raabe, Design of a twinning-induced plasticity high entropy alloy, Acta Mater. 94 (2015) 124-133.

[25] M.J. Yao, K.G. Pradeep, C.C. Tasan, D. Raabe, A novel, single phase, non-equiatomic FeMnNiCoCr high-entropy alloy with exceptional phase stability and tensile ductility, Scr. Mater.72-73 (2014) 5-8.

[26] B. Gludovatz, A. Hohenwarter, D. Catoor, E.H. Chang, E.P. George, R.O. Ritchie, A fracture-resistant high-entropy alloy for cryogenic applications, Science, 345 (2014) 1153-1158.

[27] Y. Zou, S. Maiti, W. Steurer, R. Spolenak, Size-dependent plasticity in an Nb25Mo25Ta25W25 refractory high-entropy alloy, Acta Mater. 65 (2014) 85-97.

[28] W.-R. Wang, W.-L. Wang, S.-C. Wang, Y.-C. Tsai, C.-H. Lai, J.-W. Yeh, Effects of Al addition on the microstructure and mechanical property of AlxCoCrFeNi high-entropy alloys, Intermetallics, 26 (2012) 44-51.

[29] Y. Lu, Y. Dong, S. Guo, L. Jiang, H. Kang, T. Wang, B. Wen, Z. Wang, J. Jie, Z. Cao, H. Ruan, T. Li, A promising new class of high-temperature alloys: eutectic high-entropy alloys, Sci Rep, 4 (2014) 6200.

[30] I. Basu, V. Ocelík, J.T. De Hosson, BCC-FCC interfacial effects on plasticity and strengthening mechanisms in high entropy alloys, Acta Mater. 157 (2018) 83-95.

[31] A.M. Giwa, P.K. Liaw, K.A. Dahmen, J.R. Greer, Microstructure and small-scale size effects in plasticity of individual phases of Al0.7CoCrFeNi High Entropy alloy, Extreme Mechanics Letters, 8 (2016) 220-228.

[32] K.R. Lim, K.S. Lee, J.S. Lee, J.Y. Kim, H.J. Chang, Y.S. Na, Dual-phase high-entropy alloys for high-temperature structural applications, J. Alloys Compd. 728 (2017) 1235-1238.

[33] H.X. Zhu, N.A. Fleck, A.C.F. Cocks, A.G. Evans, Numerical simulations of crack formation from pegs in thermal barrier systems with NiCoCrAlY bond coats, Mater. Sci. Eng. A. 404 (2005) 26-32.

[34] T.M. Butler, M.L. Weaver, Oxidation behavior of arc melted AlCoCrFeNi multi-component high-entropy alloys, J. Alloys Compd. 674 (2016) 229-244.

[35] T.M. Butler, M.L. Weaver, Investigation of the phase stabilities in AlNiCoCrFe high entropy alloys, J. Alloys Compd. 691 (2017) 119-129.

[36] J.A. Nychka, D.R. Clarke, Quantification of Aluminum Outward Diffusion During Oxidation of FeCrAl Alloys, Oxid. Met. 63 (2005) 325-352.

[37] R. Voytovych, I. MacLaren, M.A. Gülgün, R.M. Cannon, M. Rühle, The effect of yttrium on densification and grain growth in α-alumina, Acta Mater. 50 (2002) 3453-3463.

[38] C. Zhao, Y. Zhou, Z. Zou, L. Luo, X. Zhao, F. Guo, P. Xiao, Effect of alloyed Lu, Hf and Cr on the oxidation and spallation behavior of NiAl, Corros. Sci. 126 (2017) 334-343.

[39] B.A. Pint, K.L. More, I.G. Wright, Effect of Quaternary Additions on the Oxidation Behavior of Hf-Doped NiAl, Oxid. Met. 59 (2003) 257-283.

[40] J. Lu, H. Zhang, Y. Chen, X. Zhao, F. Guo, P. Xiao, Effect of microstructure of a NiCoCrAlY coating fabricated by high-velocity air fuel on the isothermal oxidation, Corros. Sci. 159 (2019) 108126.

[41] F. Cao, B. Tryon, C.J. Torbet, T.M. Pollock, Microstructural evolution and failure characteristics of a NiCoCrAlY bond coat in “hot spot” cyclic oxidation, Acta Mater. 57 (2009) 3885-3894.

[42] T.J. Nijdam, W.G. Sloof, Effect of Y Distribution on the Oxidation Kinetics of NiCoCrAlY Bond Coat Alloys, Oxid. Met. 69 (2007) 1-12.

[43] A. Gil, D. Naumenko, R. Vassen, J. Toscano, M. Subanovic, L. Singheiser, W.J. Quadakkers, Y-rich oxide distribution in plasma sprayed MCrAlY-coatings studied by SEM with a cathodoluminescence detector and Raman spectroscopy, Surf. Coat. Technol. 204 (2009) 531-538.

[44] A.G. Evans, D.R. Mumm, J.W. Hutchinson, G.H. Meier, F.S. Pettit, Mechanisms

controlling the durability of thermal barrier coatings, Prog. Mater. Sci. 46 (2001) 505-553.

[45] T. Xu, S. Faulhaber, C. Mercer, M. Maloney, A. Evans, Observations and analyses of failure mechanisms in thermal barrier systems with two phase bond coats based on NiCoCrAlY, Acta Mater. 52 (2004) 1439-1450.

[46] M. Subanovic, D. Naumenko, M. Kamruddin, G. Meier, L. Singheiser, W.J. Quadakkers, Blistering of MCrAlY-coatings in H2/H2O-atmospheres, Corros. Sci. 51 (2009) 446-450.

[47] R.J. Christensen, V.K. Tolpygo, D.R. Clarke, The influence of the reactive element yttrium on the stress in alumina scales formed by oxidation, Acta Mater. 45 (1997) 1761-1766.

[48] T.J. Nijdam, C. Kwakernaak, W.G. Sloof, The effects of alloy microstructure refinement on the short-term thermal oxidation of NiCoCrAlY alloys, Metall. Mater. Trans. A. 37 (2006) 683-693.

[49] C. Kwakernaak, W.G. Sloof, T.J. Nijdam, Microstructure refinement of NiCoCrAlY alloys by laser surface melting, Metall. Mater. Trans. A. 37 (2006) 695-703.

[50] C. Mennicke, M.Y. He, D.R. Clarke, J.S. Smith, The role of secondary oxide inclusions (“pegs”) on the spalling resistance of oxide films, Acta Mater. 48 (2000) 2941-2949.

[51] J.W. Hutchinson, M.Y. He, A.G. Evans, The influence of imperfections on the nucleation and propagation of buckling driven delaminations, J. Mech. Phys. Solids. 48 (2000) 709-734.

[52] J. Lu, Y. Chen, C. Zhao, H. Zhang, L. Luo, B. Xu, X. Zhao, F. Guo, P. Xiao, Significantly improving the oxidation and spallation resistance of a MCrAlY alloy by controlling the distribution of yttrium, Corros. Sci. 153 (2019) 178-190.

[53] J. Liu, J.W. Byeon, Y.H. Sohn, Effects of phase constituents/microstructure of thermally grown oxide on the failure of EB-PVD thermal barrier coating with NiCoCrAlY bond coat, Surf. Coat. Technol. 200 (2006) 5869-5876.

[54] D.R. Mumm, A.G. Evans, On the role of imperfections in the failure of a thermal

barrier coating made by electron beam deposition, Acta Mater. 48 (2000) 1815-1827.
[55] R. Molins, I. Rouzou, P. Hou, A TEM study of sulfur distribution in oxidized Ni40Al and its effect on oxide growth and adherence, Mater. Sci. Eng. A. 454-455 (2007) 80-88.
[56] P.Y. Hou, K.F. McCarty, Surface and interface segregation in β-NiAl with and without Pt addition, Scr. Mater.54 (2006) 937-941.
[57] M. Bai, H. Jiang, Y. Chen, Y. Chen, C. Grovenor, X. Zhao, P. Xiao, Migration of sulphur in thermal barrier coatings during heat treatment, Mater. Des. 97 (2016) 364-371.
[58] D. Naumenko, B.A. Pint, W.J. Quadakkers, Current Thoughts on Reactive Element Effects in Alumina-Forming Systems: In Memory of John Stringer, Oxid. Met. 86 (2016) 1-43.
[59] Z. Wěiss, K. Marshall, Elemental depth profiling of coated and surface-modified materials by GD-OES: hard coatings on cutting tools, Thin Solid Films, 308-309 (1997) 382-388.
[60] R.W. Jackson, D.M. Lipkin, T.M. Pollock, Thermal barrier coating adherence to Hf-modified B2 NiAl bond coatings, Acta Mater. 80 (2014) 39-47.
[61] H.J. Grabke, D. Wiemer, H. Viefhaus, Segregation of sulfur during growth of oxide scales,Appl. Surf. Sci. 47 (1991) 243-250.
[62] P.Y. Hou, J. Stringer, Oxide scale adhesion and impurity segregation at the scale/metal interface, Oxid. Met. 38 (1992) 323-345.
[63] B.A. Pint, Experimental observations in support of the dynamic-segregation theory to explain the reactive-element effect, Oxid. Met. 45 (1996) 1-37.
[64] H. Peng, H. Guo, J. He, S. Gong, Cyclic oxidation and diffusion barrier behaviors of oxides dispersed NiCoCrAlY coatings, J. Alloys Compd. 502 (2010) 411-416.